Supporting Information for:

Biphosphor Carbon Dots/ Chlorophyll System Entirely Derived from Chlorella microalgae for Luminescent Solar Concentrators

Filipe M. Santos,[1,*] Tiago A. G. Duarte,[2,‡] Sandra F. H. Correia,[3,‡] Rui F. P. Pereira,[4,‡] Alexandra Conde,[5] Álvaro R. Ribeiro,[6] Susana Santos Braga,[7] Sónia P. M. Ventura,[5] Rute A. S. Ferreira,[8] Verónica de Zea Bermudez,[2, 6] Sílvia C. Nunes[1, 9]

[1] FibEnTech - Fiber Materials and Environmental Technologies, Universidade da Beira Interior, 6201-001 Covilhã, Portugal;

[2] CQ-VR, Universidade de Trás-os-Montes e Alto Douro, 5000-801 Vila Real, Portugal;

[3] Instituto de Telecomunicações, Universidade de Aveiro, Campus de Santiago, 3810-193 Aveiro, Portugal

[4] Chemistry Centre and Chemistry Department, Universidade do Minho, 4710-057 Braga, Portugal;

[5] Department of Chemistry, CICECO—Aveiro Institute of Materials, Universidade de Aveiro, Campus de Santiago, 3810-193 Aveiro, Portugal;

[6] Department of Chemistry, Universidade de Trás-os-Montes e Alto Douro, 5000-801 Vila Real, Portugal;

[7] LAQV-REQUIMTE, Department of Chemistry, University of Aveiro, Campus de Santiago, 3810-193 Aveiro, Portugal;

[8] Department of Physics, CICECO—Aveiro Institute of Materials, Universidade de Aveiro, Campus de Santiago, 3810-193 Aveiro, Portugal;

[9] Department of Chemistry, Universidade da Beira Interior, 6201-001 Covilhã, Portugal;

Contents

Color codes:

Yellow: added content

Blue: content moved from the manuscript

CHARACTERIZATION OF THE AA: ChCl (16:1) SOLVENT

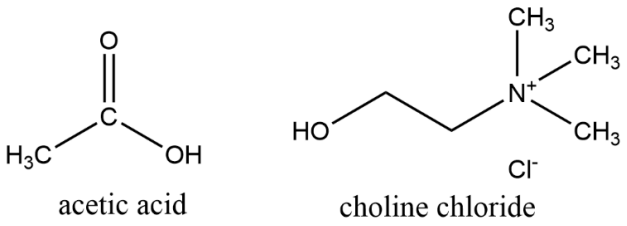

Figure S1. Molecular structures of AA and ChCl, the precursors of the used AA:ChCl (16:1) solvent used.

Thermal characterization

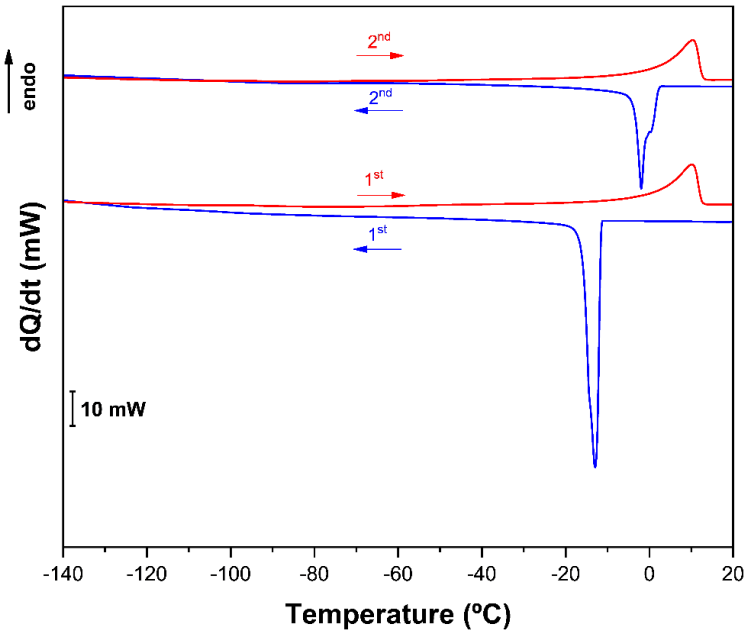

Figure S2. DSC curves for the AA:ChCl (16:1) ES.

The obtained DSC curve allowed the identification of a melting peak at about 10.00 °C (10.06 and 10.36 °C, for the first and second runs respectively) (**Figure S2**, red and yellow lines), reflecting the predominance of the AA fraction in the solvent (the melting temperatures of AA and ChCl are 16.6-16.8 and 414 ± 9 °C, respectively).[1-3] Even so, the closeness of the melting peak at 10.00 ºC with the freezing point (-1.92 °C) (**Figure S2**, blue line), strongly suggests that although the AA:ChCl (16:1) prepared in this work is beyond the eutectic point, it remains close enough for this system to

still be considered an eutectic mixture. The only study in the literature for the AA:ChCl eutectic phase diagram, reports on an AA mol fraction, χ, of *ca.* 0.7 and a corresponding melting temperature of -9 °C,[4] which agrees with the above discussion. Likewise, the experimental eutectic temperatures reported in the literature for this system are consistently below -30 °C for a 2:1 molar ratio,[5, 6] again while considering a higher ChCl proportion.

Infrared Spectroscopy Characterization

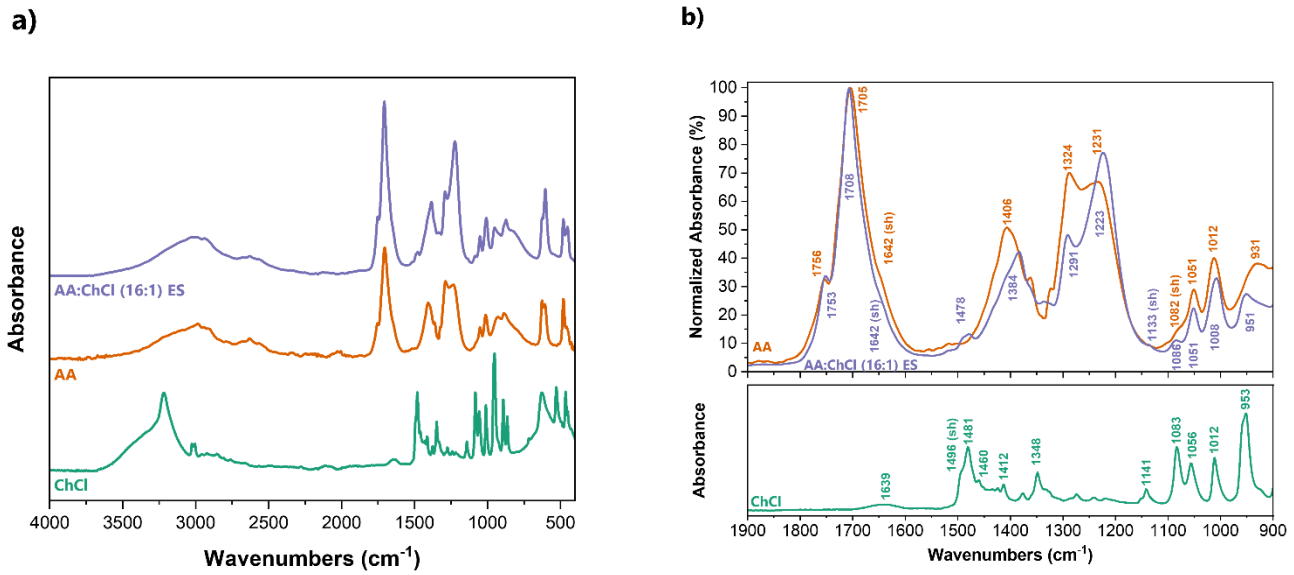

Figure S3. ATR-FTIR spectra of the AA:ChCl (16:1) ES (in purple), along with its precursors, AA (in orange) and ChCl (in green). **a)** 4000-400 cm^{-1} interval; **b) (top)** Normalized ATR-FTIR spectra for both AA and the AA:ChCl (16:1), and **(bottom)** the ATR-FTIR spectrum of the ChCl precursor in the 1900 – 1100 cm^{-1} interval.

The ATR-FTIR spectra of both precursors, as well as the prepared AA:ChCl (16:1) solvent in the 1900 – 1100 cm^{-1} interval are presented in **Figure S3**, and all band assignments have been collected in **Table S1**.

Overall, the obtained ATR-FTIR spectra for the AA and the AA:ChCl (16:1) ES are markedly similar (**Figure S3**), reflecting the high content in AA (which accounts for about 94% of the mixture). Furthermore, the ChCl moiety is known to produce very few bands in infrared spectra after ES formation[7]. The only bands observed in the AA:ChCl (16:1) spectrum originating from the ChCl

precursor were centered at 1478 and 1086 cm^{-1} (**Figure 2b(top)**, purple line), which are ascribed to the $-CH_2$ bending and the −C−C−O asymmetric stretching vibration modes, respectively.[5, 7, 8]

In the high-frequency region, both the solvent and AA spectra present a broad band (> 1000 cm^{-1} bandwidth) system encompassing both the OH/CH region (**Figure S2a** and **Table S1**). This band arises from the anharmonic resonances within the overlapping OH/CH stretching bands characteristic of carboxylic acids. It indicates the presence of a system of hydrogen bonds between AA molecules to form a dimeric unit.[9, 10] Evidence for the existence of both the dimeric and monomeric forms in equilibrium is further confirmed by the presence of two bands in the carboxyl region (1753 and 1708 cm^{-1} for the monomeric and dimeric forms (**Figure S2b(top)**, orange line). [9-11] The observation of practically unaltered bands in the same region of the solvent spectrum (**Figure S2b(top)**, purple line) indicates that apparently the −C=O groups remain unaffected by the addition of ChCl. The bands located at around 1290 cm^{-1} in both of these spectra correspond to C−O bond stretching, while the bands centered at 1406 and 1384 cm^{-1} (for AA and the AA:ChCl (16:1) spectra, respectively) arise from the contribution of the in-plane deformation vibration mode of the C−O−H group, characteristic of carboxylic acid dimers with the deformation of the CH_2 and CH_3 groups present in either the AA or the solvent. [9-12] The downshift of the AA band at 1406 cm^{-1} to 1384 cm^{-1} shows that stronger hydrogen bonds exist in the AA:ChCl (16:1). Similar shifts have been observed in infrared studies concerning the interaction of AA and water in more diluted solutions, always with an increase in the population of hydrogen bonds.[9, 13] Lastly, the vibration at 1082 cm^{-1}, related to $-CH_2CH_2-O$ stretching vibration in ChCl, remains practically unchanged in the AA:ChCl (16:1) spectra (**Table S1**), suggesting that the local chemical environment of the cholinium cation, Ch^+, has not changed with the addition of the organic acid.[14] Some authors have reported a small downward shift from 1092 to 1084 cm^{-1} in the 2:1 molar ratio for mixtures of AA:ChCl, correlating this change with the formation of hydrogen bonds involving the Ch^+ cation. [14, 15] Thus, the lack of changes in the $-CH_2CH_2-O$ stretching vibration of the Ch^+ cation suggests that any hydrogen bonds established between the precursors are formed through the Cl^- anion, as observed in other carboxylic acid/ ChCl ES mixtures. [14, 16]

Table S1. Selected band assignments for the infrared vibrations modes discussed throughout this work. ν: stretching vibration, δ: bending vibration, ρ: rocking vibration; asym.: asymmetric; sym: symmetric.

Band assignment	ChCl (cm^{-1})	DES (cm^{-1})	AA (cm^{-1})	CDS (cm^{-1})	CDCS (cm^{-1})
ν(OH)	3218 (s)				3221 (s)
ν(OH), ν(CH) anharmonic resonance		3625-2220 (br)	3640-2280 (br)	3704-2318 (br)	
ν(C-H)	3025 (w); 3006 (w)				3018 (w); 3000(w)
ν(C=O)		1753 (w); 1708 (vs)	1756 (w); 1705 (vs)	1741 (s); 1643 (s)	1741 (s)
δ(OH, water)	1639 (br)	1642 (sh)	1642 (sh)		
ν(C=C)				1475 (s)	1569 (s)
δ_{asym}(OH), δ(CH_2, scissoring) and δ_{sym}(CH_3) overtone/combination modes	1496 (sh); 1481 (s)	1478 (w); 1384 (br)	1406 (m)	1409 (m); 1382 (m)	1481; 1409 (br)
δ (CH_2, waggin) or ν ((CH_3)N, -twisting)	1412 (m); 1348 (m)				
ν_{asym} (C–O)		1291 (w), 1224 (s)	1289 (m), 1231 (m)	1241 (s)	1230 (s)
ν(C–N)	1141 (m)	1133 (sh)		1122 (s)	
ν_{asym}(C–C–O)	1083 (m)	1086 (w)	1082 (sh)	1078 (m)	1081 (m)
ρ (CH_3)	1056 (m)	1050 (m)	1051 (m)	1056 (sh)	1051 (m)
ρ (CH_3)	1012 (s)	1008 (s)	1012 (m)	1008 (m)	1010 (m)
δ_{sym}(OH) C-C stretching vibration in Ch+	953 (vs)	951 (m)	931 (m)	954 (m)	954 (m)
ν(C–C)	892 (m)		885 (m)		891 (m)
δρ		873 (m)		879 (m)	
C–N+ (symmetric stretching)	864 (m)				864 (m)

CDCS CHARACTERIZATION

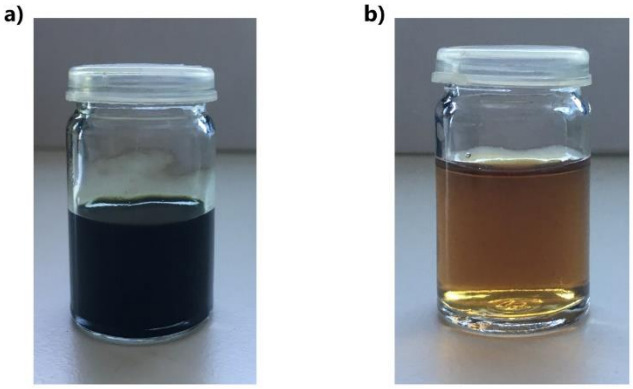

Figure S4. Photographs of the *C. pyrenoidosa* AA:ChCl (16:1) extract (left) and the CDCS system (right).

Infrared Spectroscopy Characterization

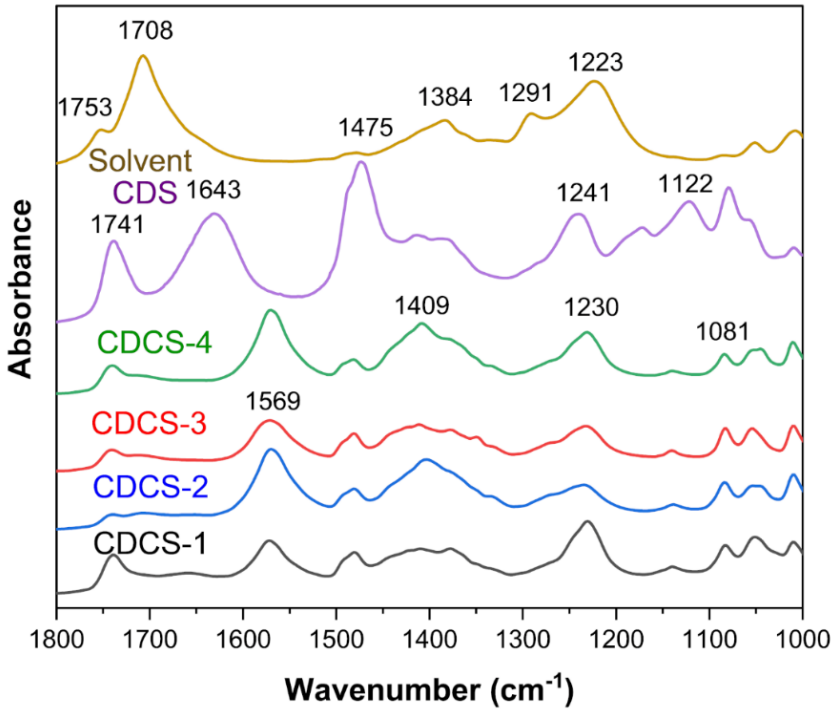

Figure S5. ATR-FTIR spectra for lyophilized CDCS-1 (black line), CDCS-2 (blue line), CDCS-3 (red line), CDCS-4 (green line), CDS (violet line) and AA:ChCl (16:1) solvent (golden line) in the 1800 – 1000 cm^{-1} region. The CDCS materials vary in the solid-liquid ratio, meaning the mass of *C. pyrenoidosa* per mL of solvent; thus, CDCS-1 and CDCS-2 were obtained by mixing 1g of *C. pyrenoidosa* in 15 mL of solvent; CDCS-3 and CDCS-4, were obtained by mixing 1.5g of *C. pyrenoidosa* in 15 mL of solvent.

The ATR-FTIR spectra of the various materials prepared by MW carbonization are represented in **Figure S5**. The band assignments have been collected in **Table S1**. Overall, the bands related to the occurrence of the Ch^+ cation are identified in the spectra of all of the synthesis attempts (**Figure S5** and **Table S1**), indicating that this cation was not completely consumed during the MW process. A band centered at 1741 cm^{-1} is detected in all the spectra except in that of the solvent (**Figure S5**, golden line**)**. This band is assigned to the C=O stretching vibration of the ester functional group and replaces the two bands relative to the C=O stretching vibration of AA at 1753 and 1708 cm^{-1}. The emergence of this band, which is more intense for CDS (**Figure S5**, violet line), than for the CDCS samples **(Figure S5**, black, blue, red, and green lines), signals the formation of acetylcholinium,[17, 18] a reaction known to happen at temperatures above 60 ºC between AA and ChCl.[19, 20] The existence of acetylcholinium is further confirmed by the presence of two other bands at 1122 and 1081 cm^{-1} from the ester function, due to C–O stretching vibration and the $–CH_2$ bending vibration, respectively (**Figure S5,** violet line). Likewise, the bands at 1291 and 1223 cm^{-1}—previously assigned to AA vibration modes— could also be attributed to the formation of the acetylcholinium cation (**Table S1**).[17, 18] Besides the formation of the acetylcholinium cation, the CDS spectrum also exhibits two bands at 1643 and 1475 cm^{-1} (**Figure S5,** violet line), which are associated with the C=O asymmetric and symmetric stretching vibration modes, and represent another fingerprint of the acetate group. The presence of this anion was to be expected, given the excess of AA on this system regarding the ChCl moiety, and arises from the neutralization of the resulting solutions, after carbonization, with NaOH.

As for the CDCS spectra (**Figure S5**, black, blue, red, and green lines), all of the prepared samples display identical spectra, regardless of the biomass/solvent ratios. The presence of acetylcholinium cation is also confirmed for these samples, given the presence of the bands at 1741 and 1081 cm^{-1}. However, no bands were found that could confirm the presence of acetate in solution. This absence of bands due to the acetate group suggests either the consumption of the excess AA present in the reaction or the formation of additional esters with other entities containing –OH groups that can be formed during biomass carbonization.

It is now worth discussing the band observed at 1409 cm^{-1} in the ATR-FTIR spectra of the four CDCS samples (**Figure S5**, black, blue, red, and green lines), and in that of the CDS (**Figure S5**, violet line), but not detected in the spectrum of the AA:ChCl (16:1) (**Figure S5** golden line). Based on the discussion presented for the AA:ChCl (16:1) ES, the band at 1384 cm^{-1} in the ATR-FTIR spectrum of AA:ChCl (16:1) ES was considered to be the result of the downshift of the 1409 cm^{-1} band and a manifestation of the establishment of hydrogen bonds between the AA and the ChCl moieties. That could also be the case here if there were more signs to corroborate the presence of AA. As it is, this

band will be assigned to the C-H bending vibration from acetylcholinium and the acetate entities, as previously reported elsewhere. [17, 18]

Finally, it should be mentioned that a new band is discerned at 1569 cm^{-1} in the ATR-FTIR spectra of all the CDCS samples (**Figure S5**, black, blue, red, and green lines). This band—characteristic of sp^2 carbon structures—is assigned to the C=C stretching vibration mode, and could be a fingerprint of the CDs.[21] In the case of CDS (Figure 3. violet line), this band appears as a shoulder, suggesting that a minor amount of CDs exist in this material.

Structural characterization

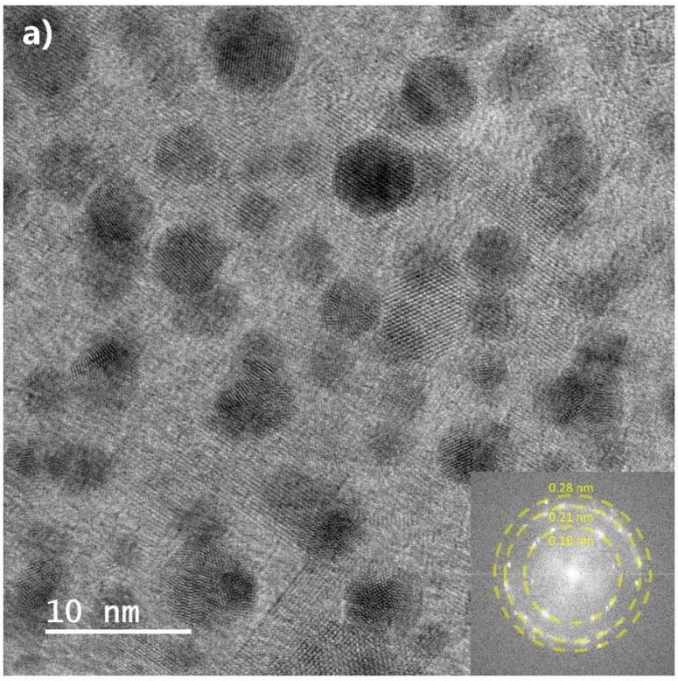

Figure S6. TEM images of CDCS sample showing lattice fringes with *d*-spacings of 0.18, 0.21 and 0.28 nm. Inset image show the FFT image with the identified of the determined *d*-spacings.

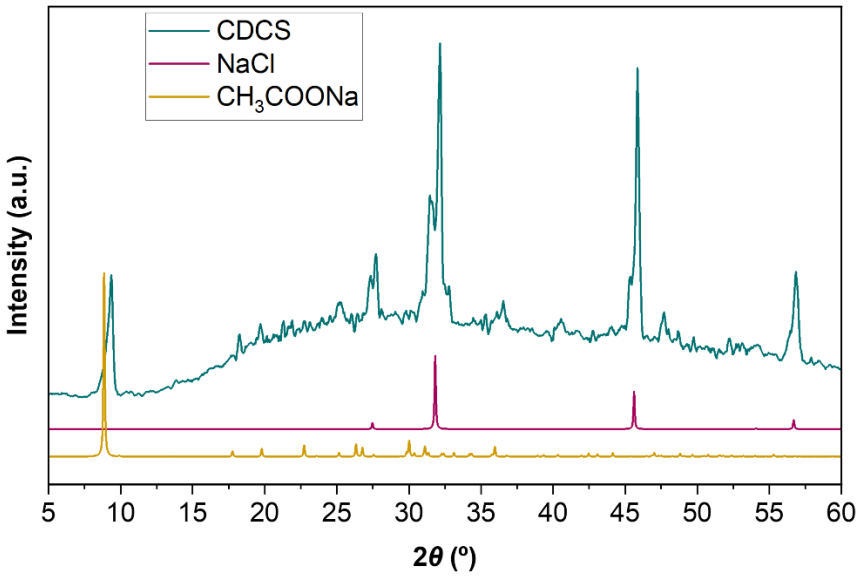

Figure S7. Powder x-ray diffraction pattern of the CDCS lyophilized sample (in green). Below are the simulated powder x-ray diffractograms for the sodium chloride (in pink) and the sodium acetate (in gold), directly obtained from their monocrystal data (CCDC deposition numbers: 1113903 and 1597740).

The powder x-ray diffractograms show a set of sharp intense peaks which have been attributed to the presence of sodium chloride (NaCl) (peaks located at 2θ: 26.6, 32.1, 45.8 and 56.7 º) and sodium acetate (CH_3COONa) (for the peaks located at 2θ: 9.3, 25.2 and 36.4 º). An additional set of peaks, centered at 2θ 27.3, 31.4 and 45.2 have also been assigned to NaCl, although in this case, to a secondary more distorted crystallization phase.

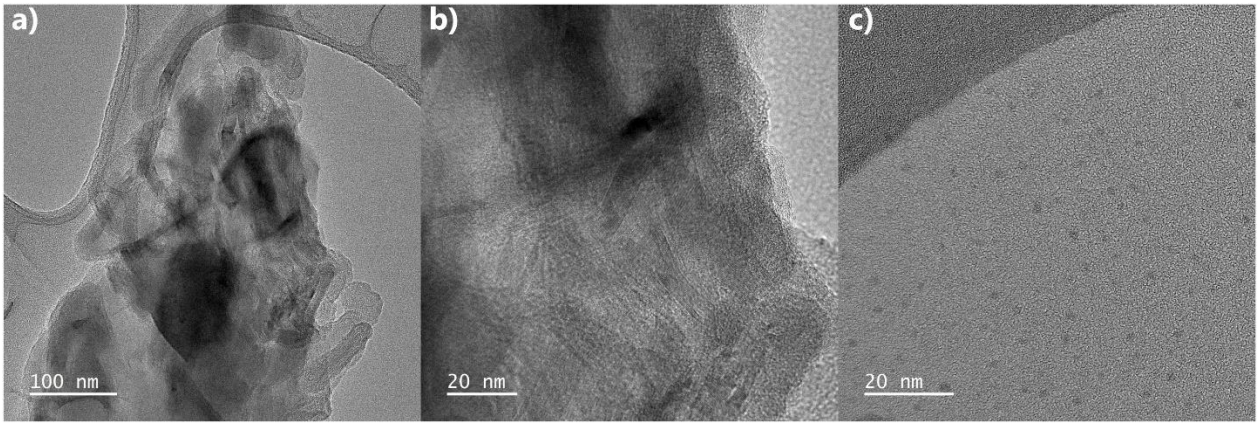

Figure S8. High-resolution TEM images obtained from the CDS sample.

Thermal Characterization

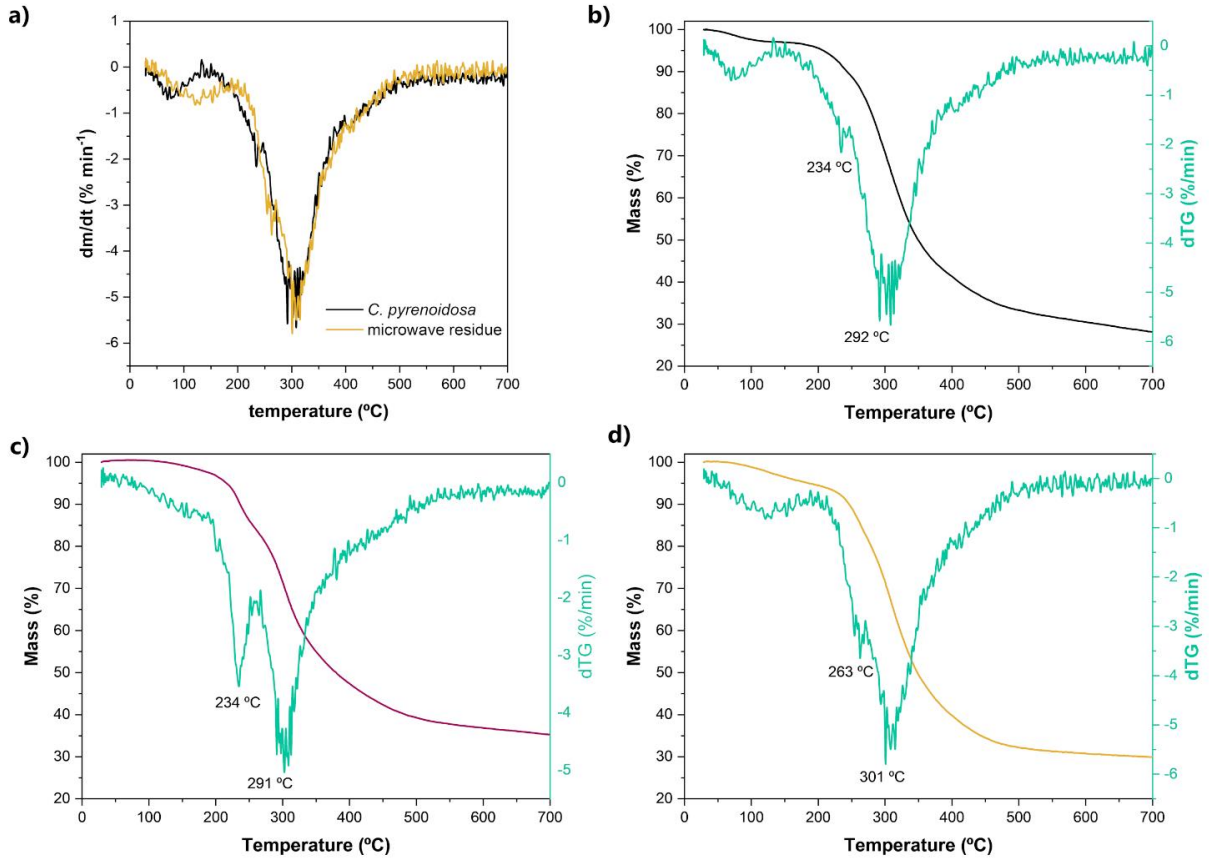

Figure S9. DTGA curves: **a)** comparison of the curves obtained for the *C. pyernoidosa* biomass and the MW residue; **b)** *C. pyrenoidosa*; **c)** extract residue and **d)** MW residue.

Table S2. Mass loss (%) and peak temperature results of TGA /DGTA data

Degradation events	***C. pyrenoidosa***		**Extract residue**		**Microwave residue**	
	Mass loss (%)	Peak temperature (ºC)	Mass loss (%)	Peak temperature (ºC)	Mass loss (%)	Peak temperature (ºC)
Stage 1	3.04	70	1.90		5.16	121
Stage 2 (carbohydrates)	7.25	234	12.79	234; 265	11.02	265
Stage 2 (proteins)	43.02	292	35.40	291	40.95	301
Stage 3	18.52		15		13.03	
Residual mass	28.17		34.91		29.84	

Optical characterization

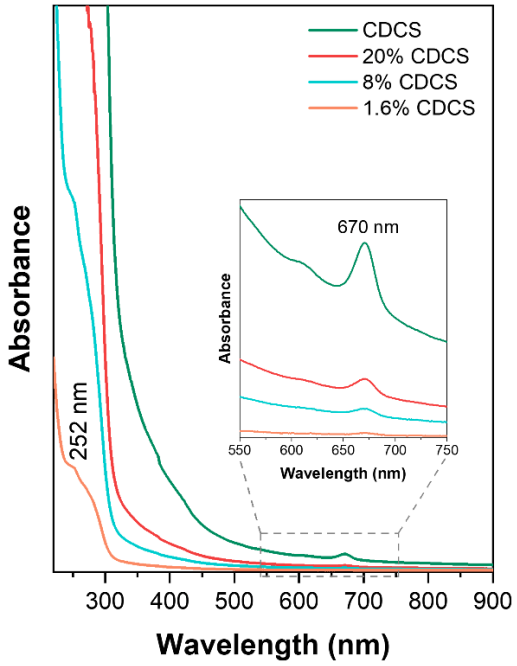

Figure S10. UV-vis absorption spectra of the CDCS.

OPTICAL PROPERTIES OF CDS

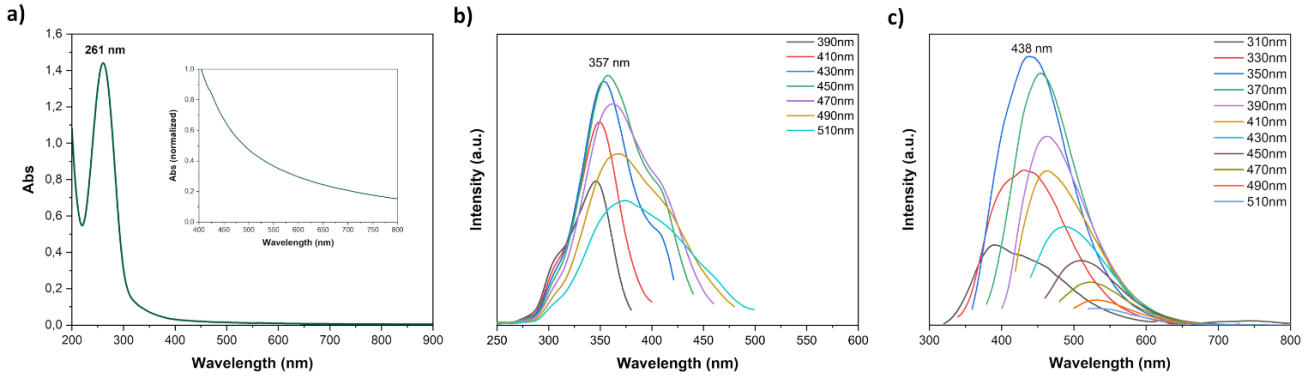

Figure S11. Optical properties of CDS. **a)** UV-vis absorption spectrum; **b)** PL excitation spectra; **c)** PL emission spectra.

CHL DEGRADATION PRODUCTS

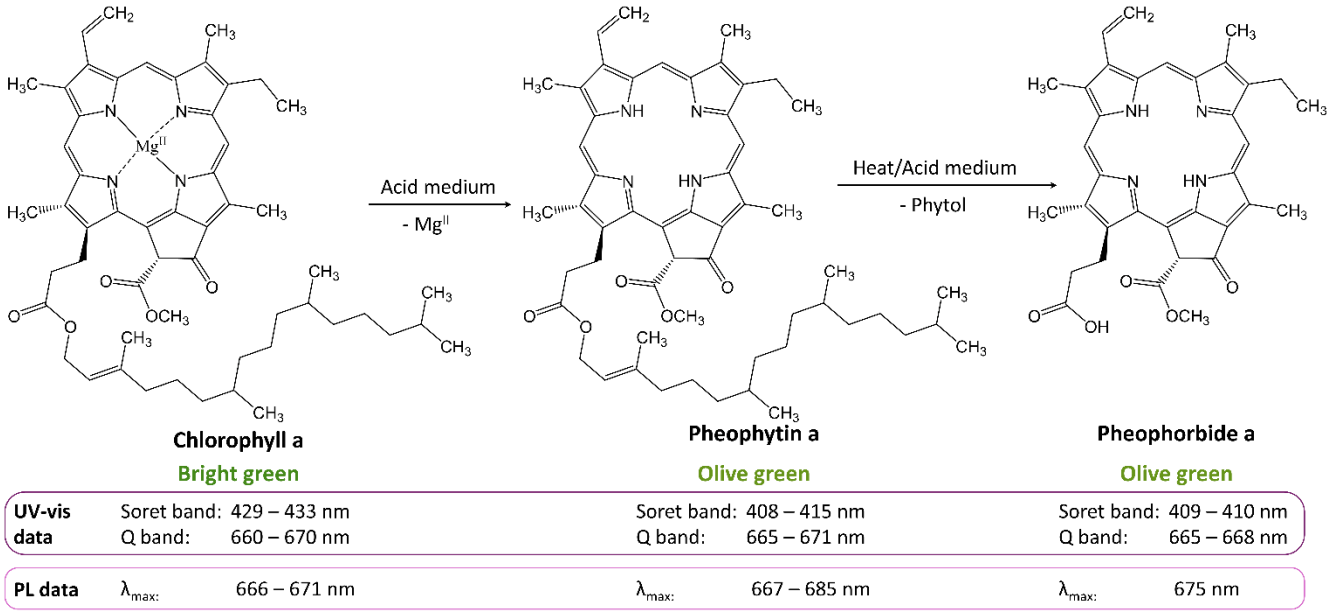

Figure S12. Chl-a (left) and its degradation products after acid and heat treatment. The UV-vis absorption and the fluorescence spectral data were taken from ref. 22.

CD FORMATION FROM THE CHL EXTRACT

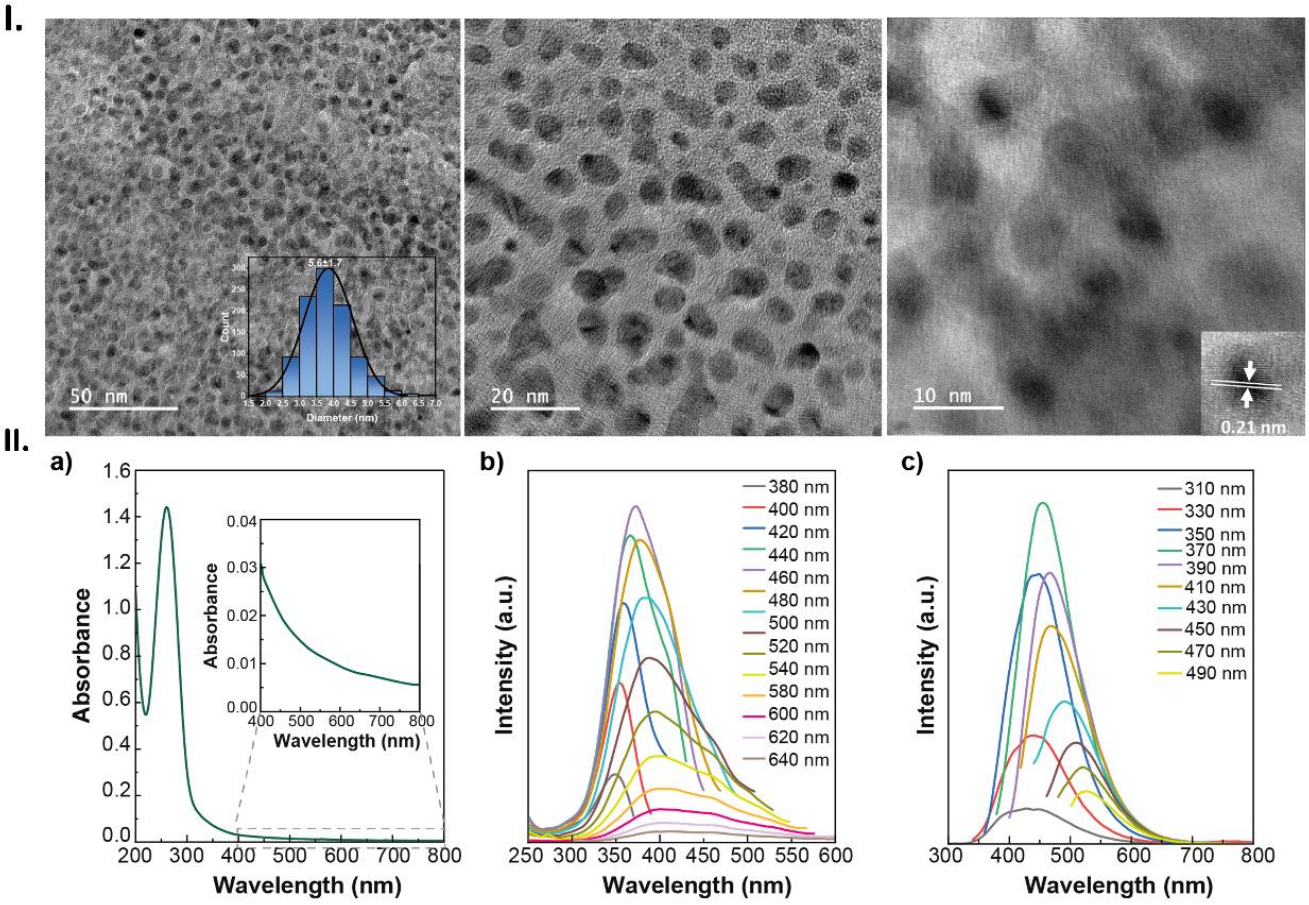

Figure S13. CDs prepared from a chlorophyll extract dissolved in our AA:ChCl (16:1). I. HR-TEM images of the CDs obtained from this sample: inset of a) shows the size distribution; inset of c) shows the lattice fringes and characteristic d-spacing; II. Optical properties of the CDs in aqueous solution: a) UV-vis spectrum; b) excitation and c) emission spectrum. The inset in a) shows the visible region of the spectrum of the same CDs' aqueous solution.

OPTICAL PROPERTIES OF WATER – PEG MIXTURES

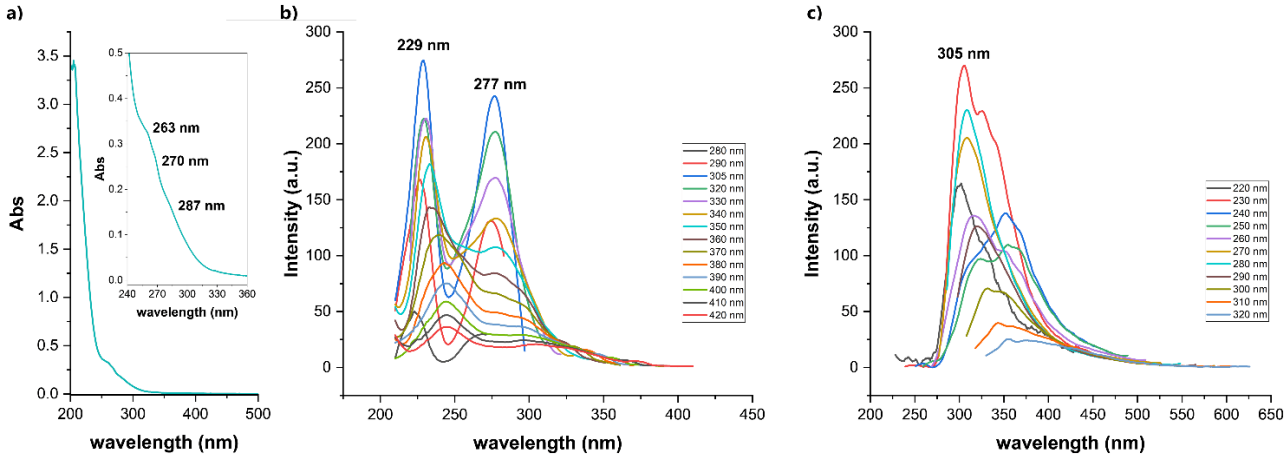

Figure S14. PEG-200 Optical properties: **a)** UV-vis absorption spectrum; **b)** PL excitation spectra; **c)** PL emission spectra.

Table S3. PL data for the water / PEG-200 CDCS solutions.

Water / PEG(200) solutions			**PEG-200 fraction**		**CDs PL**		
m(H_2O)	**m(PEG-200)**	**m(Total)**	**%**	**χ**	**maximum excitation wavelength**	**maximum emission wavelength**	**Stokes shift**
(g)	**(g)**	**(g)**	**(w/w)**	**(mol/mol)**	**(nm)**	**(nm)**	**(nm)**
5	0.0	5.0	0	0	472	542	70
5	0.52	5.52	9.3	0.01	465	536	71
5	1.01	6.01	16.8	0.02	464	534	70
5	2.01	7.01	28.6	0.04	464	530	66
5	3.04	8.04	37.8	0.05	462	529	67
5	5.02	10.02	50.1	0.08	457	528	71
5	8.02	13.02	61.6	0.13	457	525	68
5	15.02	20.02	75.0	0.21	383	464	81
5	25.01	30.01	83.4	0.31	375	450	75
5	50.02	55.02	90.9	0.48	348	432	84
0	5.51	5.51	100	1.000	469	537	68

Table S4. Emission quantum yield (Φ) values of the reported samples.

Sample		λ_{exc} (nm)	Φ
Aqueous system	CDCS	370	0.01±0.01
		450	
	CDCS 20% dilution	330	
		350	
		370	0.02±0.01
		450	
	CDCS 8% dilution	330	0.01±0.01
		370	0.02±0.01
		450	
	CDCS 1.6% dilution	330	
		370	
		450	
Water / PEG-200 solutions (w/w)	9.3% PEG	380	0.01±0.01
		465	
	16.8% PEG	380	
		460	
	28.6% PEG	380	0.02±0.01
		460	0.01±0.01
	37.8% PEG	380	
		460	
	50.1% PEG	380	0.02±0.01
		460	
	61.6% PEG	380	
		460	
	75.0% PEG	380	
		460	
	83.4% PEG	380	
		460	
	90.9% PEG	380	
		460	
PEG-200 solution	100% PEG	380	
		460	

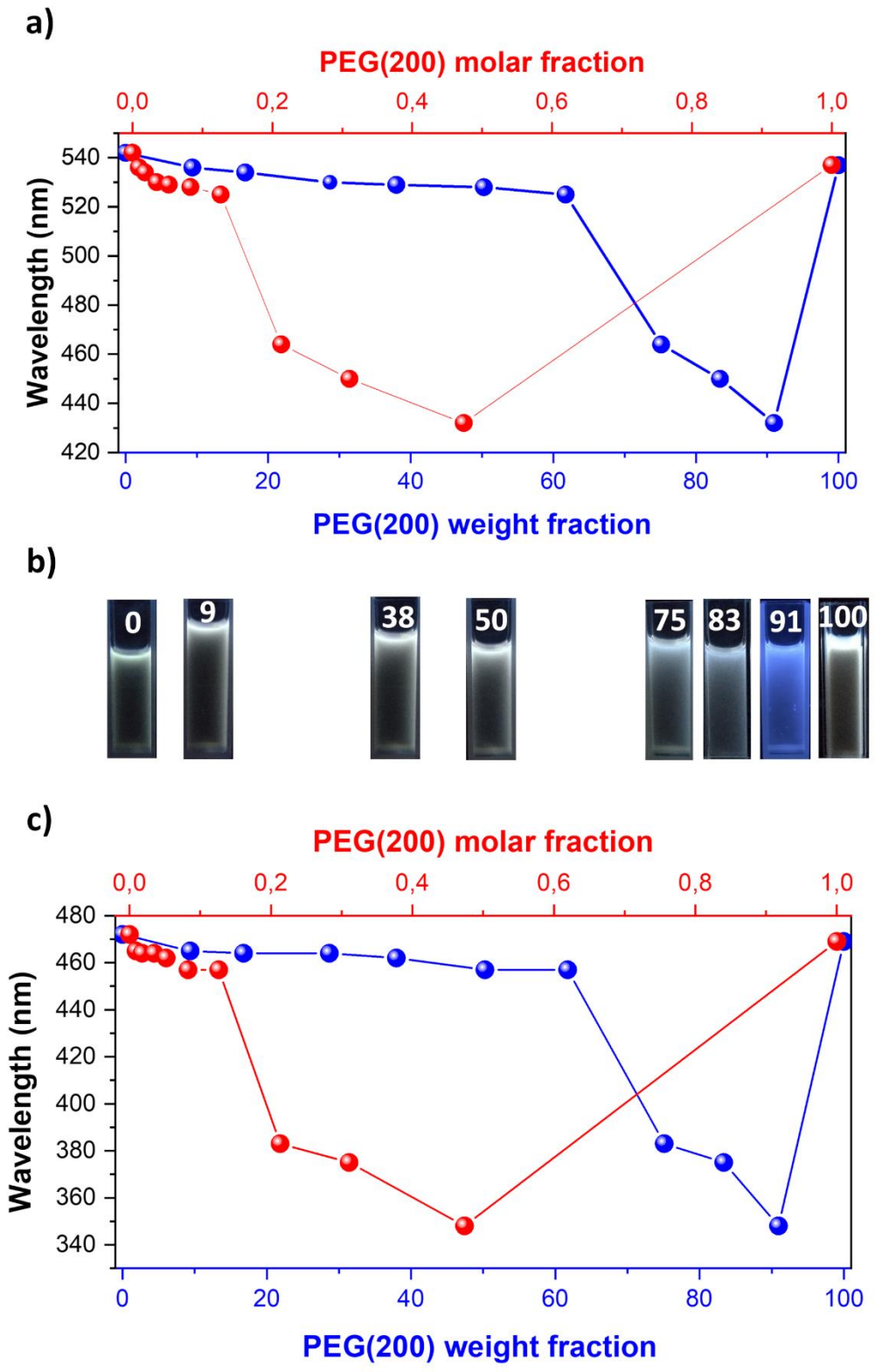

Figure S15. Variation of the **a)** the excitation and **c)** the emission maximum wavelengths with the PEG-200 weight fraction and PEG-200 molar fraction. In **b)** photographs of the prepares water/PEG-200 solutions under a 365nm lamp are presented.

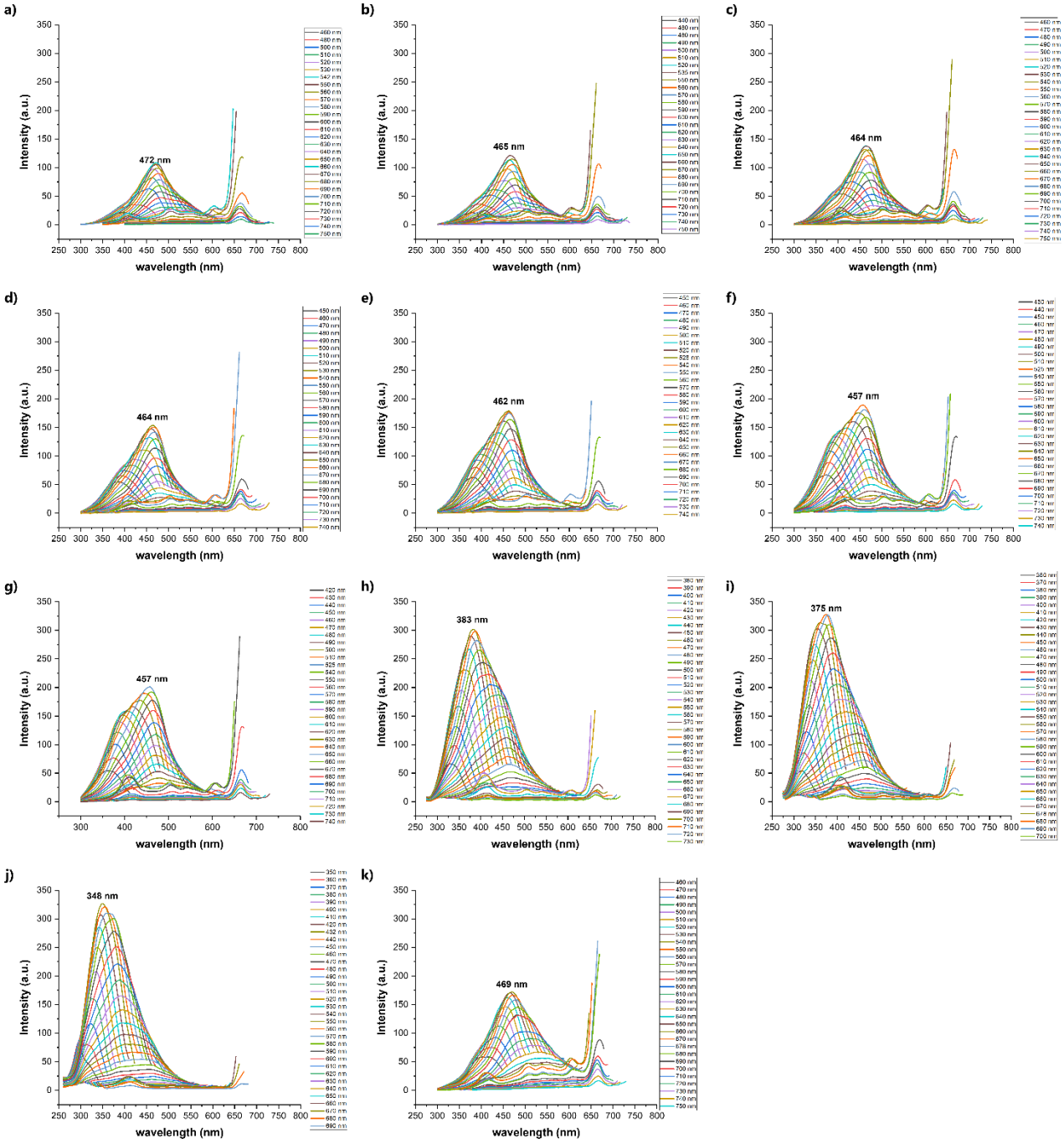

Figure S16. Excitation spectra for the various Water/PEG-200 mixture in weight ratio. **a)** 0% PEG-200; **b)** 9.09% PEG-200; **c)** 16.7% PEG-200; **d)** 28.6% PEG-200; **e)** 37.5% PEG-200; **f)** 50.0% PEG-200; **g)** 61.5% PEG-200; **h)** 75.0% PEG-200; **i)** 83.3% PEG-200; **j)** 90.9% PEG-200; **k)** 100% PEG-200

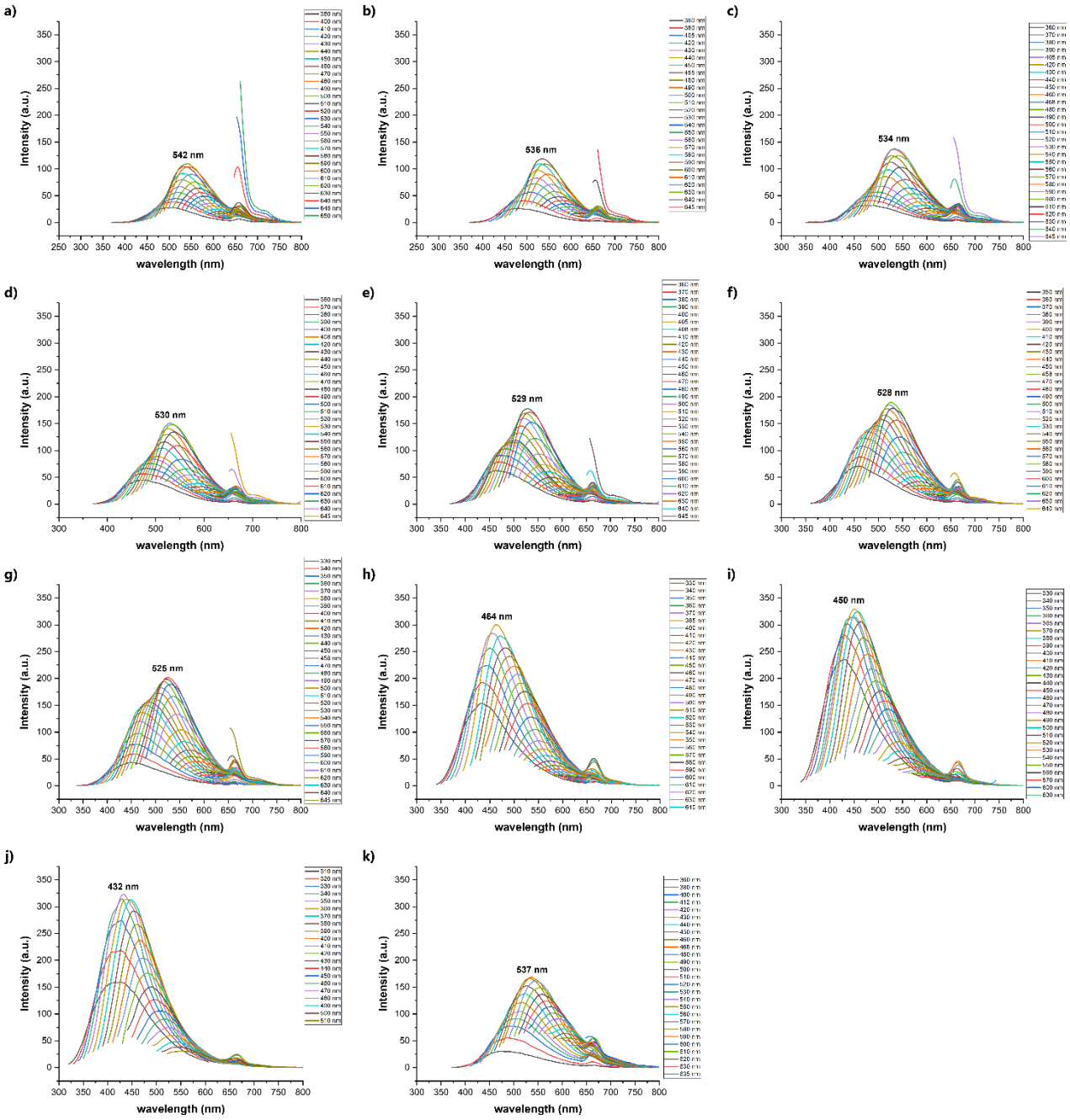

Figure S17. Emission spectra for the various Water/PEG(200) mixture in weight ratio. **a)** 0% PEG(200); **b)** 9.09% PEG-200; **c)** 16.7% PEG-200; **d)** 28.6% PEG-200; **e)** 37.5% PEG-200; **f)** 50.0% PEG-200; **g)** 61.5% PEG-200; **h)** 75.0% PEG-200; **i)** 83.3% PEG-200; **j)** 90.9% PEG-200; **k)** 100% PEG-200.

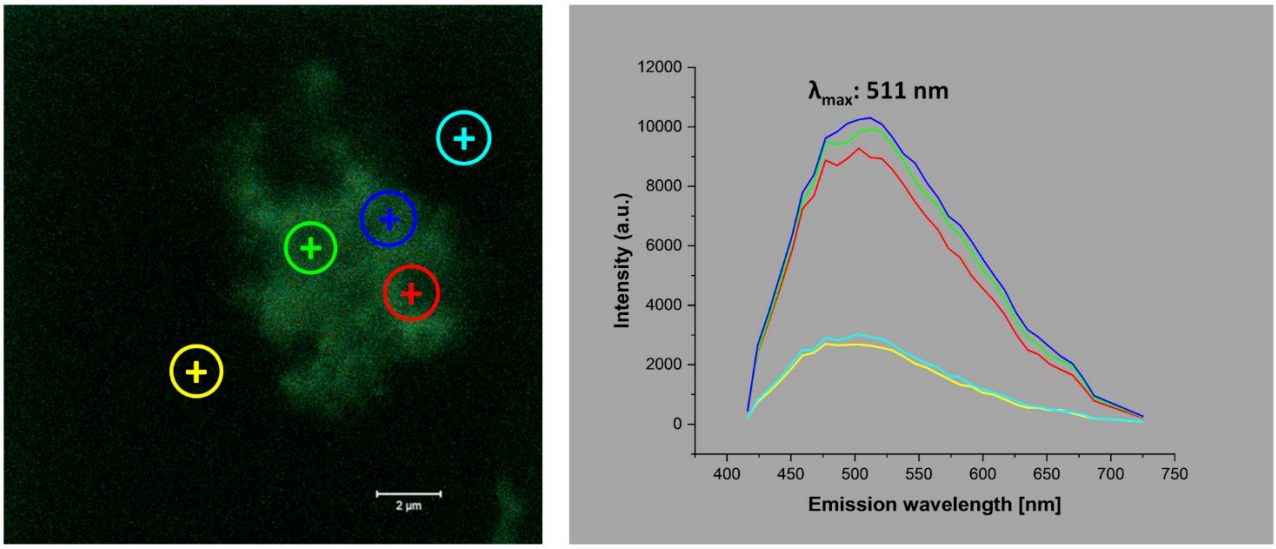

Figure S18. Confocal microscopy images of fluorometric analysis of the CDCS in the PEG-200 solution, under a solid-state laser exciting at wavelengths of 405 nm (25%) and 633 nm (100%), with the emission fluorescence profiling.

LSCS PERFORMANCE EVALUATION PARAMETERS

The optical conversion efficiency (η_{opt}) was estimated through:[23]

$$\eta_{opt} = \frac{P_{out}}{P_{in}} = \frac{I_{SC}^{L} V_{oc}^{L}}{I_{SC} V_{oc}} \frac{A_e}{A_s} \frac{\eta_{solar}}{\eta_{PV}}$$

where I_{SC}^{L} and V_{oc}^{L} represent the short-circuit current and the open-circuit voltage when the PV device is coupled to the LSC, I_{sc} and V_{oc} are the corresponding values of the PV device exposed directly to solar radiation, A_s and A_e are the exposed and total edge areas respectively, η_{solar} is the efficiency of the PV device relative to the total solar spectrum and η_{PV} is the efficiency of the PV device at the LSC emission wavelengths. Three measurements were performed for each case, with a found relative error ($\eta_{opt}/\Delta\eta_{opt}$) below 10 %.

The experimental η_{opt} values were determined by illuminating the top surface of the LSCs (4.0×2.0 cm^2) with AM1.5G illumination from a solar simulator. The optical power at the LSC output was estimated using a commercial c-Si PV panel (KXOB22-01X8F, IXYS, composed of 8 cells) coupled to one edge of the LSC while the remaining edges were covered with reflective tape (Fig. S17). The

PV cells have a total active area of 2.2x0.7 cm^2 closely matching that of the LSC edge (2.0×1.0 cm^2) to maximise light coupling. The I_{sc} and V_{oc} values were measured using a semiconductor device analyzer (B10500A, Keysight). All measurements were performed under AM1.5G illumination (1000 $W \cdot m^{-2}$) using a 150 W xenon arc lamp, class A, solar simulator (Model 10500, Abet Technologies).

The power conversion efficiency (PCE) was calculated through:

$$PCE = \frac{P_{out}^{el}}{P_{in}} = \frac{I_{SC}^{L} V_{oc}^{L} FF}{A_S \int_{\lambda_1}^{\lambda_2} I_{AM1.5G}\,(\lambda) d\lambda}$$

where P_{out}^{el} is the PV device output electrical power and FF is the fill factor, respectively.

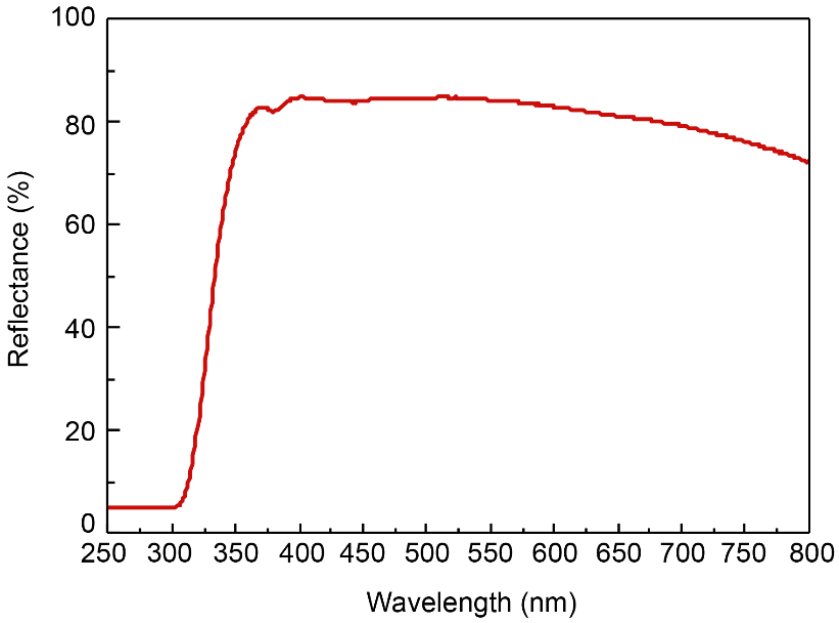

Figure S19. Reflectance curve of the reflective tape used on the LSCs.

Table S5. Overview of reported LSCs incorporating CDs as optically active centres.

Fluorophore/host	Dimensions (cm^3)	η_{opt} (%)	PCE (%)	Ref.
CDCS in water	4.0×2.0×1.0	9.4	0.17	This work
CDCS in PEG-200		10.7	0.23	
RhB-CDs/Water	2.0×2.0×1.0	5.43	0.18	24
RhB-CDs/d-U(600)	3.5×2.5×0.1	0.058	8.3×10^{-4}	
RhB-CDs/d-U(600)	*L*=3.5; *D*=0.3	1.7	0.014	
N-CDs/PMMA	2.5×1.6×0.1	4.75	3.94	25
N-CDs/PMMA	2.0×2.0×0.2	12.23	2.63	26
Si-CDs/Ormosil	3.0×3.0×0.3	12		27
N-CDs/PVP	1.8×1.8×0.1	5.02	4.97	28
CDs/PVP-CdSe/CdS/PLMA	10×10×0.2	1.4	-	29
CDs/PVP; Perovskite QDs/PLMA-co-EGDA	10×10×0.2	-	3.05	30
CDs-OLA/PLMA	10×1.5×0.2	1.2		
N-CDs/PDLC	5.0×2.5×0.4	4.52	2.49	31
CDs/PVP	10×10×1.0	0.92		32
CDs/PVP-TPFE-Rho/PMMA	2.5×2.0×0.3		4.06	33
CDs/PVP	10×10×0.9	1.6	0.7	34
Si-CDs/siloxane	3.0×3.0×0.3	3.9		35
b-CD/PVA; g-CD/PVP; r-CD/PVP+PEI [a)]	8×8×0.8	2.3		36
y-CDs/PVP	2.5×2.5×0.1	3.51	2.39	37
g-CDs/PVP		2.76	1.94	
r-CDs/PVP		2.77	1.96	
g-CDs/y-CDs/r-CDs/PVP [a)]	2.5×2.5×0.3	4.03	2.92	
Si-CDs-D1	2.5×2.5×0.1	7.58	6	38
Narrow sized CDs/PVP	15×15×0.5	2.2	1.13	39
r-CDs/PVP	10×10×0.7		1.9	40
g-CD/PVP			1.7	
r-CD/g-CD/PVP [a)]	10×10×1.4		2.3	
y-CDs/PVP	10×10×0.9	2.6	2.3	41
r-CDs/PVP		3	2.7	
y-CDs/r-CDs/PVP [a)]	10×10×0.2	4.3	3.8	
CDs/Ag/SiO_2	3.0×2.0×0.2	1.23	0.43	42
CDs/Ag/SiO_2/PVP	5.0×5.0×0.2	0.9	0.62	
b-CDs/g-CDs/PNIPAm	2.5×2.5×0.2	2.7		43
y-CDs/p(MMA-NIPAm)		5.84		44
Ba^{2+}-capped CDs/PVP	10×10×0.4	3.2	1.9	45
Ca^{2+}-capped CDs/PVP		2.9	1.7	
Si-CDs/PVP	15×15×0.5		2.06	46
Si-CDs/PVP	5.0×5.0×0.5	4.8	4.36	
OSi-CDs	2.5×2.5×0.1	4.5	0.12	47
OSi-CDs		5.89	0.16	
OSi-CDs	5.0×5.0×0.1	3.13	0.06	

Table S5 ***(cont.)*****.** Overview of reported LSCs incorporating CDs as optically active centres.

Fluorophore/host	Dimensions (cm^3)	η_{opt} (%)	PCE (%)	Ref.
DAMO-CDs/PMMA	2.0×2.0×0.5	9.3		48
y-CDs/PVP	10×10×1.0	4.56	4.1	49
BWCDs/HEMA/EGDMA	2.5×2.5×0.15	1.36		50
g-QDs/EVA	2.5×2.5×0.2	3.08		
r-QDs/EVA		2.55		
BWCDs/HEMA/EGDMA;g-QDs/EVA [a)]		1.89		
BWCDs/HEMA/EGDMA;r-QDs/EVA [a)]		2.54		
BWCDs/HEMA; g-QDs/EVA; r-QDs/EVA [a)]		3.76		

RhB-CDs – Rhodamine B-derived carbon dots; d-U(600) – di-ureasil organic-inorganic hybrid; N-CDs – nitrogen-doped carbon dots; Si-CDs – silicon-doped carbon dots; y-CDs – yellow-emitting carbon dots; b-CDs – blue-emitting carbon dots; g-CDs – green-emitting carbon dots; r-CDs – red-emitting carbon dots; OSi-CDs – organosilane carbon dots; BWCDs – blue-white emitting carbon dots; PDMS – polydimethylsiloxane;; PMMA – poly(methylmethacrylate); PVP – poly(vinylpyrrolidone); PEI – Polyethyleneimine; OLA – oleylamine; PLMA – poly(lauryl methacrylate); EGDA – Ethylene glycol diacetate; PDLC – Polymer-dispersed liquid crystals; PNIPAm – Poly(N-isopropylacrylamide); DAMO – N-[3-(trimethoxysilyl)propyl]ethylenedi-amine; HEMA – hydroxyethyl methacrylate; EGDMA – ethylene glycol dimethacrylate; [a)]Tandem LSC

BIBLIOGRAPHY

1. van den Bruinhorst, A.; Avila, J.; Rosenthal, M.; Pellegrino, A.; Burghammer, M.; Costa Gomes, M., Defying decomposition: the curious case of choline chloride. *Nature Communications* **2023,** *14* (1), 6684.
2. Nakabayashi, T.; Kosugi, K.; Nishi, N., Liquid structure of acetic acid studied by raman spectroscopy and ab initio molecular orbital calculations. *The Journal of Physical Chemistry A* **1999,** *103* (43), 8595-8603.
3. Gavezzotti, A., A molecular dynamics view of some kinetic and structural aspects of melting in the acetic acid crystal. *Journal of Molecular Structure* **1999,** *485-486*, 485-499.
4. de Almeida Pontes, P. V.; Ayumi Shiwaku, I.; Maximo, G. J.; Caldas Batista, E. A., Choline chloride-based deep eutectic solvents as potential solvent for extraction of phenolic compounds from olive leaves: extraction optimization and solvent characterization. *Food Chemistry* **2021,** *352*, 129346.
5. Ngatcha, A. D. P.; Muhammad, G.; Lv, Y.; Xiong, W.; Zhao, A.; Xu, J.; Alam, M. A., Microalgae biomass pre-treatment with deep eutectic solvent to optimize lipid isolation in biodiesel production. *Biomass Conversion and Biorefinery* **2022,** *12 (Suppl. 1)* (1), 133-143.
6. Gautam, R.; Kumar, N.; Lynam, J. G., Theoretical and experimental study of choline chloride-carboxylic acid deep eutectic solvents and their hydrogen bonds. *Journal of Molecular Structure* **2020,** *1222*, 128849.
7. Hayyan, M.; Abo-Hamad, A.; AlSaadi, M. A.; Hashim, M. A., Functionalization of graphene using deep eutectic solvents. *Nanoscale Research Letters* **2015,** *10* (1), 324.
8. Sheikh, A.; Khan, A. Y.; Ahmed, S., Physicochemical properties of choline chloride/acetic acid as a deep eutectic solvent and its binary solutions with DMSO at 298.15 to 353.15 K. *ACS Omega* **2024,** *9* (3), 3730-3745.
9. Gofurov, S.; Makhmanov, U.; Kokhkharov, A.; Ismailova, O. B., Structural and optical characteristics of aqueous solutions of acetic acid. *Applied Spectroscopy* **2019,** *73* (5), 503-510.
10. Gadermann, M.; Vollmar, D.; Signorell, R., Infrared spectroscopy of acetic acid and formic acid aerosols: pure and compound acid/ice particles. *Physical Chemistry Chemical Physics* **2007,** *9* (32), 4535-4544.

11. Max, J.-J.; Chapados, C., Infrared spectroscopy of aqueous carboxylic acids: comparison between different acids and their salts. *The Journal of Physical Chemistry A* **2004,** *108* (16), 3324-3337.
12. Muhammad, G.; Wang, J.; Xiong, W.; Lv, Y.; Zhang, S.; Zhao, A.; Jahanbakhsh-Bonab, P.; Solovchenko, A.; Xu, J.; Alam, M. A., Polyol based deep eutectic solvent-assisted pretreatment for enhanced lutein extraction from Chlorella pyrenoidosa. *Journal of Molecular Liquids* **2022,** *368*, 120775.
13. Palencia, M., Functional transformation of Fourier-transform mid-infrared spectrum for improving spectral specificity by simple algorithm based on wavelet-like functions. *Journal of Advanced Research* **2018,** *14*, 53-62.
14. Zhu, S.; Li, H.; Zhu, W.; Jiang, W.; Wang, C.; Wu, P.; Zhang, Q.; Li, H., Vibrational analysis and formation mechanism of typical deep eutectic solvents: An experimental and theoretical study. *Journal of Molecular Graphics and Modelling* **2016,** *68*, 158-175.
15. Zhu, W.; Wang, C.; Li, H.; Wu, P.; Xun, S.; Jiang, W.; Chen, Z.; Zhao, Z.; Li, H., One-pot extraction combined with metal-free photochemical aerobic oxidative desulfurization in deep eutectic solvent. *Green Chemistry* **2015,** *17* (4), 2464-2472.
16. Perkins, S. L.; Painter, P.; Colina, C. M., Experimental and computational studies of choline chloride-based deep eutectic solvents. *Journal of Chemical & Engineering Data* **2014,** *59* (11), 3652-3662.
17. Pawlukojć, A.; Hetmańczyk, Ł., INS, DFT and temperature dependent IR studies on dynamical properties of acetylcholine chloride. *Vibrational Spectroscopy* **2016,** *82*, 37-43.
18. Aslanian, D., Vibrational spectroscopic approach to the study of acetylcholine and related compounds. *Life Sciences* **1983,** *32* (25), 2809-2825.
19. Florindo, C.; Oliveira, F. S.; Rebelo, L. P. N.; Fernandes, A. M.; Marrucho, I. M., Insights into the Synthesis and Properties of Deep Eutectic Solvents Based on Cholinium Chloride and Carboxylic Acids. *ACS Sustainable Chemistry & Engineering* **2014,** *2* (10), 2416-2425.
20. Rodriguez Rodriguez, N.; van den Bruinhorst, A.; Kollau, L. J. B. M.; Kroon, M. C.; Binnemans, K., Degradation of deep-eutectic solvents based on choline chloride and carboxylic acids. *ACS Sustainable Chemistry & Engineering* **2019,** *7* (13), 11521-11528.
21. Duarte, T. A. G.; Pereira, R. F. P.; Medronho, B.; Maltseva, E. S.; Krivoshapkina, E. F.; Varela-Dopico, A.; Taboada, P.; Fu, L.; Ferreira, R. A. S.; de Zea Bermudez, V., A Glance at novel ionanofluids incorporating silk-derived carbon dots. *Chemistry of Materials* **2024,** *36* (3), 1136-1152.
22. Taniguchi, M.; Lindsey, J. S., Absorption and fluorescence spectral database of chlorophylls and analogues. *Photochemistry and Photobiology* **2021,** *97* (1), 136-165.
23. Reisfeld, R.; Shamrakov, D.; Jorgensen, C., Photostable solar concentrators based on fluorescent glass films. *Solar Energy Materials and Solar Cells* **1994,** *33* (4), 417-427.
24. Correia, S. F. H.; Fu, L.; Dias, L. M. S.; Pereira, R. F. P.; de Zea Bermudez, V.; André, P. S.; Ferreira, R. A. S., An autonomous power temperature sensor based on window-integrated transparent PV using sustainable luminescent carbon dots. *Nanoscale Advances* **2023,** *5* (13), 3428-3438.
25. Li, Y.; Miao, P.; Zhou, W.; Gong, X.; Zhao, X., N-doped carbon-dots for luminescent solar concentrators. *Journal of Materials Chemistry A* **2017,** *5* (40), 21452-21459.
26. Gong, X.; Ma, W.; Li, Y.; Zhong, L.; Li, W.; Zhao, X., Fabrication of high-performance luminescent solar concentrators using N-doped carbon dots/PMMA mixed matrix slab. *Organic Electronics* **2018,** *63*, 237-243.
27. Talite, M. J.; Huang, H.-Y.; Wu, Y.-H.; Sena, P. G.; Cai, K.-B.; Lin, T.-N.; Shen, J.-L.; Chou, W.-C.; Yuan, C.-T., Greener luminescent solar concentrators with high loading contents based on in situ cross-linked carbon nanodots for enhancing solar energy harvesting and resisting concentration-induced quenching. *ACS Applied Materials & Interfaces* **2018,** *10* (40), 34184-34192.
28. Wang, Z.; Zhao, X.; Guo, Z.; Miao, P.; Gong, X., Carbon dots based nanocomposite thin film for highly efficient luminescent solar concentrators. *Organic Electronics* **2018,** *62*, 284-289.
29. Liu, G.; Zhao, H.; Diao, F.; Ling, Z.; Wang, Y., Stable tandem luminescent solar concentrators based on CdSe/CdS quantum dots and carbon dots. *Journal of Materials Chemistry C* **2018,** *6* (37), 10059-10066.
30. Zhao, H.; Benetti, D.; Tong, X.; Zhang, H.; Zhou, Y.; Liu, G.; Ma, D.; Sun, S.; Wang, Z. M.; Wang, Y.; Rosei, F., Efficient and stable tandem luminescent solar concentrators based on carbon dots and perovskite quantum dots. *Nano Energy* **2018,** *50*, 756-765.

31. Mateen, F.; Ali, M.; Oh, H.; Hong, S.-K., Nitrogen-doped carbon quantum dot based luminescent solar concentrator coupled with polymer dispersed liquid crystal device for smart management of solar spectrum. *Solar Energy* **2019,** *178*, 48-55.
32. Zhao, H., Refractive index dependent optical property of carbon dots integrated luminescent solar concentrators. *Journal of Luminescence* **2019,** *211*, 150-156.
33. Ma, W.; Li, W.; Liu, R.; Cao, M.; Zhao, X.; Gong, X., Carbon dots and AIE molecules for highly efficient tandem luminescent solar concentrators. *Chemical Communications* **2019,** *55* (52), 7486-7489.
34. Zhao, H.; Liu, G.; Han, G., High-performance laminated luminescent solar concentrators based on colloidal carbon quantum dots. *Nanoscale Advances* **2019,** *1* (12), 4888-4894.
35. Talite, M. J.; Huang, H.-Y.; Cai, K.-B.; Capinig Co, K. C.; Cynthia Santoso, P. A.; Chang, S.-H.; Chou, W.-C.; Yuan, C.-T., Visible-transparent luminescent solar concentrators based on carbon nanodots in the siloxane matrix with ultrahigh quantum yields and optical transparency at high-loading contents. *The Journal of Physical Chemistry Letters* **2020,** *11* (2), 567-573.
36. Zdražil, L.; Kalytchuk, S.; Holá, K.; Petr, M.; Zmeškal, O.; Kment, Š.; Rogach, A. L.; Zbořil, R., A carbon dot-based tandem luminescent solar concentrator. *Nanoscale* **2020,** *12* (12), 6664-6672.
37. Wang, J.; Wang, J.; Xu, Y.; Jin, J.; Xiao, W.; Tan, D.; Li, J.; Mei, T.; Xue, L.; Wang, X., Controlled synthesis of long-wavelength multicolor-emitting carbon dots for highly efficient tandem luminescent solar concentrators. *ACS Applied Energy Materials* **2020,** *3* (12), 12230-12237.
38. Wu, J.; Xin, W.; Wu, Y.; Zhan, Y.; Li, J.; Wang, J.; Huang, S.; Wang, X., Solid-state photoluminescent silicone-carbon dots/dendrimer composites for highly efficient luminescent solar concentrators. *Chemical Engineering Journal* **2021,** *422*, 130158.
39. Zhao, H.; Liu, G.; You, S.; Camargo, F. V. d. A.; Zavelani-Rossi, M.; Wang, X.; Sun, C.; Liu, B.; Zhang, Y.; Han, G.; Vomiero, A.; Gong, X., Gram-scale synthesis of carbon quantum dots with a large Stokes shift for the fabrication of eco-friendly and high-efficiency luminescent solar concentrators. *Energy & Environmental Science* **2021,** *14* (1), 396-406.
40. Han, Y.; Zhao, X.; Vomiero, A.; Gong, X.; Zhao, H., Red and green-emitting biocompatible carbon quantum dots for efficient tandem luminescent solar concentrators. *Journal of Materials Chemistry C* **2021,** *9* (36), 12255-12262.
41. Li, J.; Zhao, H.; Zhao, X.; Gong, X., Red and yellow emissive carbon dots integrated tandem luminescent solar concentrators with significantly improved efficiency. *Nanoscale* **2021,** *13* (21), 9561-9569.
42. Liu, X.; Benetti, D.; Rosei, F., Semi-transparent luminescent solar concentrators based on plasmon-enhanced carbon dots. *Journal of Materials Chemistry A* **2021,** *9* (41), 23345-23352.
43. Xu, B.; Wang, J.; Cai, C.; Xin, W.; Wei, L.; Yang, Q.; Peng, B.; Hu, Y.; Li, J.; Wang, X. Construction of laminated luminescent solar concentrator "smart" window based on thermoresponsive polymer and carbon quantum dots *Crystals* [Online], 2022, p. 1612.
44. Xin, W.; Wang, J.; Xu, B.; Wu, J.; Wang, J.; Ren, Z.; Cai, C.; Xue, C.; Li, J.; Wang, X., Construction of highly efficient carbon dots-based polymer photonic luminescent solar concentrators with sandwich structure. *Nanotechnology* **2022,** *33* (30), 305601.
45. Liu, B.; Wang, L.; Gong, X.; Zhao, H.; Zhang, Y., Large scale synthesis of carbon dots for efficient luminescent solar concentrators. *Journal of Materials Chemistry C* **2022,** *10* (48), 18154-18163.
46. Gong, X.; Zheng, S.; Zhao, X.; Vomiero, A., Engineering high-emissive silicon-doped carbon nanodots towards efficient large-area luminescent solar concentrators. *Nano Energy* **2022,** *101*, 107617.
47. Wu, Y.; Zhan, Y.; Xin, W.; Cao, W.; Li, J.; Chen, M.; Jiang, X.; Wang, J.; Sun, Z., Highly Emissive Carbon Dots/Organosilicon Composites for Efficient and Stable Luminescent Solar Concentrators. *ACS Applied Energy Materials* **2022,** *5* (2), 1781-1792.
48. Gao, L.; Wang, C.; Xu, S.; Xia, P.; Liu, F.; Sun, H.; Wang, Z.; Lu, C.; Cui, Y., Free Radical-Resistant Carbon Dots for Bulky Luminescent Solar Concentrators with High Optical Efficiency. *ACS Applied Nano Materials* **2022,** *5* (6), 7850-7857.
49. Li, J.; Zhao, H.; Zhao, X.; Gong, X., Boosting efficiency of luminescent solar concentrators using ultra-bright carbon dots with large Stokes shift. *Nanoscale Horizons* **2023,** *8* (1), 83-94.

50. Cai, C.; Wang, M.; Wang, J.; Xu, B.; Wang, J.; Zhang, L.; Xin, W.; Xue, L.; Li, J.; Wang, X., Efficiently boosting the optical performances of laminated luminescent solar concentrators via combing blue-white light-emitting carbon dots and green/red emitting perovskite quantum dots. *Applied Surface Science* **2023,** *609*, 155313.